Available online at www.sciencedirect.com

SCIENCE DIRECT®

Surface & Coatings Technology 190 (2005) 171–189

SURFACE & COATINGS TECHNOLOGY

www.elsevier.com/locate/surfcoat

Rolling contact fatigue of post-treated WC–NiCrBSi thermal spray coatings

S. Stewart[a], R. Ahmed[a,*], T. Itsukaichi[b]

[a] Department of Mechanical and Chemical Engineering, Heriot Watt University, Riccarton, Edinburgh, Scotland, UK

[b] Fujimi Inc., 82-28 Kakamihigashi-machi-5, Kakamigahara, Gifuken 509-0103, Japan

Received 22 July 2003; accepted in revised form 5 April 2004

Abstract

The aim of this experimental study was to comprehend the relative rolling contact fatigue (RCF) performance and failure modes of functional graded WC–NiCrBSi thermal spray coatings in the as-sprayed and post processed state, by means of Hot Isostatic Pressing (HIPing) and vacuum heating. Functional graded WC–NiCrBSi coatings were deposited by a JP5000 system. HIPing was carried out at two different furnace temperatures of 850 and 1200 °C, while vacuum heating was performed at the elevated temperature of 1200 °C. The rate of heating and cooling was kept constant at 4 °C/min. Rolling contact fatigue tests were conducted using a modified four ball machine under various tribological conditions of contact stress and configuration, in full film elasto hydrodynamic lubrication. Results are discussed in terms of the relative RCF performance of the as-sprayed and post-treated coatings, and also surface and sub-surface examination of rolling elements using scanning electron microscope (SEM), light microscope and surface interferometry.

Test results reveal that performance of the coating was dependant on the microstructural changes due to post-treatment. Coatings heat-treated at 1200 °C displayed superior performance in RCF testing over the as-sprayed coatings at all stress levels (2, 2.3, 2.7 GPa) with emphasis on RCF performance at lower stress load of 2 GPa, where no failure occurred. Improvement in RCF performance was attributed to the diffusion between the carbides and matrix resulting in improved strength. At higher levels of contact stress, failure was surface initiated, and was attributed to initiation and propagation of micro-cracks at the edge of rolling contact region which led to coating delamination.

Keywords: Thermal spray; Hot isostatic pressing; Rolling contact fatigue; Failure modes

1. Introduction

There is an ever-increasing demand in the surface engineering industry to improve the operating performance of components, while maintaining or reducing the manufacturing costs. In many types of industrial appliances such as gears, camshafts and rolling element bearings, surface damage generated by rolling/sliding contact limits the life of the components and hence reduces durability and product reliability. This drives the development and implementation of state of the art surface coatings which can enable improved life reliability and load bearing capacity in more hostile environments.

Thermal spray coatings deposited by techniques such as the Detonation Gun (D-Gun), High Velocity Oxy Fuel (HVOF) and arc wire are used in many industrial applications requiring abrasion, sliding, fretting and erosion resistance. However, even using state of the art coating systems, it is not possible to achieve defect free thermal spray coatings. Difficulties arise due to the mismatch in elastic modulus, thermal expansion coefficients and hardness between the surface layer and the substrate material. This leads to the generation of residual stresses, which not only form during coating deposition but also arise during contact loading, and over time can cause coating delamination [1] and hence limit the use of thermal spray coatings to low stress applications. Voort [2] initially showed that thermal spray coatings not only have significant porosity but also secondary phase particles and a lack of fusion, which will not be eliminated using the FGM approach [3]. There are two kinds of pore geometry in thermal spray coatings, introduced by different mechanisms. One is lamellar poros-

* Corresponding author. Tel.: +44-131-451-4722; fax: +44-131-451-3129.

E-mail address: R.Ahmed@hw.ac.uk (R. Ahmed).

0257-8972/$ - see front matter © 2004 Elsevier B.V. All rights reserved.
doi:10.1016/j.surfcoat.2004.04.059

ity (elongated pores) at the lamellar or splat boundaries which is believed to arise from intermittent contact. The other types of pores are normally spherical in shape and arise from the expansion of trapped gases.

By applying a post-treatment, thermal spray coatings can be made more attractive to industry. Previous investigations have reported significant improvements in the coating microstructure at high Hot Isostatic Pressing (HIPing) temperatures [4]. The interlamellar porosity is completely eliminated while spherical pores, approximately 2 μm in diameter, are reduced to microvoids less than 0.1 μm in size. HIPing involves placing batches of coated samples inside a furnace which is contained within a pressure vessel. Temperatures of 1500 °C are possible while pressures of up to 200 MPa can be applied for a certain period of time. The coated samples are normally encapsulated in order to prevent surface cracking which can occur from the harsh conditions imposed by the HIPing process. However, this safety precaution technically restricts the shape and size of the samples which could be HIPed. Since emphasis in thermal spray technology is to continually search for cost effective solutions, an important objective in this analysis was to successfully HIP the coated samples without encapsulation. The principal aim of this investigation was to comprehend the relative rolling contact fatigue (RCF) performance and failure modes of functional graded WC–NiCrBSi thermal spray coatings in as-sprayed and post processed state.

Vacuum heating is another method of post-treatment which is similar to HIPing, but without the pressure, and can have a significant influence on the tribological performance of HVOF coatings [5]. At elevated temperatures, vacuum heating reduces porosity and oxide content within the microstructure, which results in increased coating densification and hardness [6]. Published research on vacuum heating is limited. Guo et al. [7] investigated the effect of vacuum heating on WC–NiCrBSi coatings. Results indicated that as well as a reduction in oxide content, porosity, micro-cracks and non-bond zones, porosity of the coating changed from continuous to discontinuous. The grains of the second phase became finer and more dispersive, and therefore, internal stress was decreased and improved by distribution. It was also indicated using Auger electron spectrometry that the NiCr binder diffused from the substrate to the coating. Hence in this investigation, in addition to the HIPing post-treatment, vacuum heating was also used to compare the relative performance and failure modes of as-sprayed and post-treated functional graded WC–NiCrBSi coatings.

Hence, by improving metallurgical bonding at splat and substrate interface levels, elimination of amorphous phases and micro-cracks as well as uniform compressive residual stress through out the coating microstructure [8], this can benefit both existing and novel industrial applications of thermal spray and HIPing in areas including rollers, shafts, drilling, mining equipment and especially harsh tribological environments such as the oil and chemical industry. To date, limited investigations exist on the influence of post-treatment on fatigue and delamination resistance in rolling/sliding contact [9]. In this study, functional graded WC–NiCrBSi coated discs were HIPed under the condition of the temperature range from 850 to 1200 °C and the pressure of 100 MPa. A number of coatings were also vacuum heated at 1200 °C, incorporating identical conditions of heating and cooling. A modified four-ball machine, which differs from the four-ball machine in the sense that the lower planetary balls are free to rotate was used to investigate the rolling contact fatigue performance under different tribological conditions. The failed rolling element coatings were analysed for surface failures using scanning electron microscope (SEM) and light microscope observations. The results are discussed with the help of micro-hardness measurements, indentation modulus analysis and surface interferometry.

2. Experimental procedure

2.1. Sample preparation

2.1.1. Powder processing and thermal spraying

Two types of agglomerated and sintered powders were prepared for the deposition of the functional graded coating. Specialised nickel alloy powder of composition Ni–7.56%Cr–3.69%Si–2.57%Fe–1.55%B–0.25%C and WC carbides less than 5 μm in size were manufactured to spray the graded coating. The powder-manufacturing route involved pre-alloying the powders which led to the formation of a spray-dried and sintered composite which was then sprayed onto the substrates. Pre-alloying has a number of inherent advantages over the other powder-manufacturing routes, e.g. mechanical blending. With mechanical blending, WC particles do not melt within the gun and hence on contact with the substrate rebound reducing the deposit efficiency. In sintered and agglomerated powders, deposit efficiency is thus significantly higher. Segregation during spraying leads to differences in specific gravity and particle size of each original powder with blending, hence, it is difficult to achieve a uniform structure in mechanically blended powders. The optimal route of pre alloying leads to a homogeneous structure. Coatings were deposited on 440-C bearing steel substrates with JP5000 HVOF system. Prior to the coating process , the substrate material was shot-blasted and preheated to increase the contact area for mechanical interlock and decrease the quenching stresses associated with the impacting lamella. Spraying was carried out using Kerosene as the fuel gas and oxygen as the powder carrier gas. The gun was kept fixed at a spray distance of 380 mm and the barrel length was measured at 4 in. The FGM consisted of two uniformed layers of approximately the same thickness. The FGM coating was graded from WC–40%Ni alloy to WC–10%Ni alloy on the surface. The average coating thickness of the WC–40%Ni alloy was 100 μm while the upper layer of WC–10%Ni alloy after grinding and polishing was 300 μm.

2.1.2. Post-treatment

Coated substrates were Hot Isostatically Pressed (HIPed) at two different temperatures of 850 and 1200 °C. Due to the technical and economical restrictions imposed by the encapsulated HIPing process, as explained earlier in Section 1, the coatings were HIPed in unencapsulated conditions. As opposed to previous studies on HIPing of thermal spray coatings, e.g. by Khor et al. [10,11], where HIPing was carried out in encapsulated conditions due to surface porosity, recent advances in HVOF systems, which are capable of producing coatings with negligible porosity, have thus made it possible to HIP thermal spray coatings without encapsulation. Successful HIPing of thermal spray cermet coatings in unencapsulated conditions thus offer technically and economically attractive industrial solutions to improve coating performance.

The choice of HIPing temperature was based on the premise that the lower temperature would give minimum distortion to the substrate material, while the higher temperature would be beneficial for the microstructural transformation of the coating material. This is consistent with the findings by Nerz et al. [12] where microstructure changes were reported at about 850 °C. In addition, DTA analysis of the spraying powders displayed an exothermic reaction occurring at 831 °C and around 1100 °C. Changes referring to the heating and cooling rate for both cycles were kept constant at 4 °C/min in order to prevent surface cracking. A constant pressure of 100 MPa on the samples was maintained for 1 h by Argon gas being pressurised against the surface of the discs. Under these conditions, none of the coatings exhibited any signs of surface cracking.

In order to investigate the influence of pressure on the microstructure of thermal spray coatings, a number of coated substrates were also vacuum heated at 1200 °C in unencapsulated conditions. The heating and cooling rate was kept constant at 4 °C/min in order to prevent surface cracking.

2.2. Rolling contact fatigue (RCF) tests

To study the fatigue of highly loaded machine elements such as roller bearings and gears, which are subjected to a combined rolling/sliding motion, extensive tests have to be performed. Since test results of rolling contact fatigue investigations exhibit extensive scatter, many tests are necessary to determine the fatigue life with statistical confidence. It is also difficult to explain the influence of separate parameters on the results because the working conditions of machine elements in industrial practice are not constant. Therefore, test rigs with specimens of simple form are favoured to investigate the influence of single parameters on fatigue life. Tourret et al. [13] have investigated a number of variations on the standard four-ball machine such as types I, II, III configurations. A number of recent studies have successfully incorporated the type II configuration to test the RCF performance of PVD and thermal spray-coated balls and cones [14]. Due to the hostile environment of the heat treatment, it can be difficult to HIP drive balls or cones. Therefore, in the current investigation, steel discs 31 mm in diameter were fabricated, coated and then HIPed. Hence, in changing the shape of the rolling drive element, a number of other modifications to the four ball machine were necessary in order to maintain the correct rolling/sliding kinematics. These modifications will be discussed in Section 2.2.1.

A schematic of the modified four-ball machine is shown in Fig. 1. In the current set-up of the assembly, the coated disc was assembled to the drive shaft via a collet and drove the three planetary balls, which act as the rolling elements in the configuration of the deep groove ball bearing. The stationary cup represents the outer race of the rolling element ball bearing in the contact model of the modified four-ball machine. A ceramic ball was placed below the three planetary balls which prevented the planetary balls contacting during testing.

The coated discs were ground and polished to attain a Root Mean Square (RMS) surface roughness of 0.065 ± 0.015 μm (R_q). Planetary rolling element balls were commercial grade 12.7-mm diameter 440-C bearing steel or hot isostatically pressed silicon nitride ceramic with a surface roughness of 0.01 ± 0.015 μm (R_q). RCF tests were conducted under immersed lubrication conditions at a spindle speed (ω) of 4000 + 10 rpm and at an ambient temperature of 24 °C. Failure was defined as the increase in vibration amplitude above a pre-set level. Vitrea 320, a high viscosity hydrocarbon oil, was used during the RCF tests. The ratio (λ) of the Elasto-hydrodynamic Lubricant (EHL) film thickness to the average surface roughness was calculated using the following relationship;

$$\lambda = \left\{ \frac{H_{\min}}{(R_{qd}^2 + R_{qp}^2)^{0.5}} \right\} \quad (1)$$

where R_{qd} was the RMS surface roughness of the driving rolling element disc. R_{qp} was the RMS surface roughness of the planetary balls. $H_{\min}$ was the minimum film thickness and calculated using the following relationship of hard Elasto-hydrodynamic Lubrication;

$$H_{\min} = 3.63 U^{0.68} G^{0.49} W^{-0.073} (1 - e^{-0.68k}) \quad (2)$$

U is the dimensionless speed parameter, G is the dimensionless elliptically material parameter, W is the dimensionless load parameter and k is the dimensionless elliptically parameter. The λ value was approximated greater than three for Vitrea 320 lubricant thus indicating full film regime.

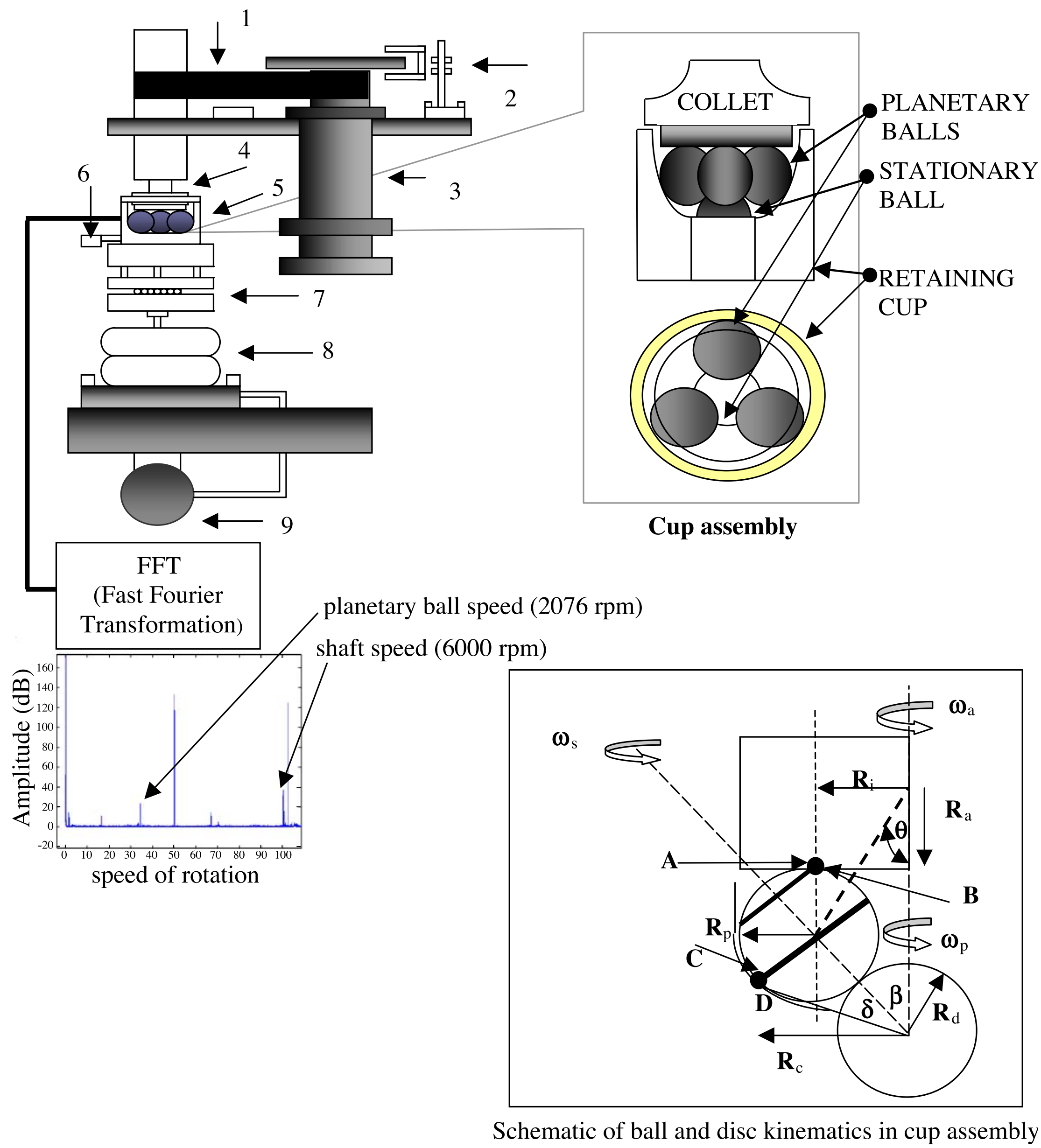

Fig. 1. Schematic of the modified four-ball machine ($R_i = 7.75$ mm $R_p = 6.35$ mm, $\theta = 36.83°$, $\beta = 37.61°$, $\delta = 31.16°$, $\omega = 4000 \pm 10$ rpm). (1, Belt drive; 2, speed sensor; 3, spindle driving motor; 4, coated disc and collet; 5, cup assembly; 6, thermocouple; 7, thrust bearing; 8, bellows; 9, pressure gauge).

2.2.1. Ball kinematics

The kinematics analysis in the cup assembly of the modified rolling contact fatigue machine can enable a better understanding of the fatigue mechanisms by providing an insight to the surface velocities, micro-slip and sliding within the contact region. In rolling contacts, the phenomena of micro-slip within the contact area of contacting bodies, either due to material deformation or due to differences in the Young's modulus and lubricant traction, can be significantly affected by the kinematics. The objective of the following analysis was thus to calculate the angular and linear velocities of the coated drive disc and the driven rolling elements for the experimental contact geometry, and then evaluate the micro-slip due to the contact deformation of the materials. This was achieved by considering the instantaneous velocities of the drive plate and the driven rolling elements. Tests were to be continuously run for 70 million stress cycles since it has been shown in published literature that this is a practical benchmark for resistance to rolling contact fatigue [15]. The number of stress cycles per revolution of the drive shaft, also known as the stress cycle factor, was calculated from the contact kinematics equations.

The kinematics of the rolling contact fatigue machine as shown in Fig. 1 display an example in which the rolling motion is associated with the spin. The three planetary balls orbit about the axis of rotation of the plate and have a spin component at an angle to the axis of rotation. From this figure, it can be appreciated that:

$$\delta = \{(\mathrm{arcTan}(R_c/R_d\cos\beta)) - \beta\}$$

$$\theta = \mathrm{arcTan}\{(R_i)/(R_a + R_p)\}$$

$$\beta = \arcsin\{(\sqrt{(R_i^2 + (R_a + R_p)^2})\sin\theta/(R_p + R_d)\}$$

also

$$\omega = (2\pi N)/60$$

The instantaneous velocity at the drive plate at point a (V_a) can be given as:

$$V_a = \omega_a \times R_i \quad (3)$$

Consider the motion of the planetary ball at point b. The motion can be divided into two components. These are; about the vertical axis MN and about an axis inclined at an angle β to the vertical. The instantaneous velocity of the planetary ball at point b (V_b) can be given as:

$$V_b = \omega_p R_i + \omega_s(\cos(90 - \beta))R_p \quad (4)$$

Assuming no slip at the contact of the drive plate and the driven ball:

$$V_a = V_b$$

Equating Eqs. (3) and (4) leads to;

$$\omega_a \times R_i = \omega_p R_i + \omega_s(\cos(90 - \beta))R_p \quad (5)$$

Consider the motion of the planetary ball at point c. The instantaneous velocity at point c (V_c) is given by:

$$V_c = \omega_p R_c + (-)\omega_s((1/3R_c)(\cos\beta)) \quad (6)$$

Assuming no slip between the planetary ball and the cup at point c,d

$$V_c = V_d$$

But $V_d = 0$

Hence

$$\omega_s = \omega_p R_c/(1/3R_c)(\cos\beta) \quad (7)$$

substituting Eq. (7) into Eq. (5) leads to:

$$(\omega_a/\omega_p) = R_i + ((R_c/(1/3R_c)(\cos\beta))((\cos(90 - \beta))R_p)) = 2.89 \quad (8)$$

Therefore, a shaft speed $\omega_a = 628.32$ rads/s (6000 rpm); angular speed of planetary balls $\omega_p = 217.41$ rads/s (2076 rpm). The number of stress cycles per revolution of the shaft can be calculated as : Number of stress cycles/revolution $= Z(\omega_a - \omega_p)/\omega_a$. Substituting in Eq. (8) gives:

$$\text{Stress Cycle Factor} = Z1 - (1/(R_i + (((1/3R_c)/(\cos\beta)) \times ((\cos(90 - \beta))R_p)) = 1.96 \quad (9)$$

2.2.2. FFT analysis

Analytical studies to calculate the speed of the lower planetary balls under a given shaft speed and configuration of the modified four ball system (above) are generally made under the assumption of pure rolling conditions in the four ball assembly. However, depending upon the tribological conditions such as friction and lubricant behaviour, the actual speeds can be different from the theoretically calculated speeds. Hence, experimental investigation of the orbital speed of the lower planetary balls cannot only reveal whether the motion was pure rolling or a combination of pure rolling and sliding, but can also estimate the amount of sliding in the four ball system by comparing the results of experimental investigations with the theoretical calculations.

In order to experimentally investigate the orbital speeds, an accelerometer was connected to the body of the cup assembly. The signal from the accelerometer was relayed to an amplifier. The amplified signal was fed into a computer where dedicated software converted the signal to a digital reading. The data were then processed by Matlab in which using the Fast Fourier Transformation (FFT) technique, the data were converted to the frequency domain. The technique enabled the precise measurement of the drive shaft speed and average speed of the planetary balls. Fig. 1 shows the results recorded at a shaft speed of 6000 rpm (100 Hz) where the average speed of the planetary balls was 2076 rpm (34 Hz), providing further verification of the kinematics analysis previously shown in Section 2.2.1.

2.2.3. Slip analysis due to contact conformity

The applied load changes the initial point contact into a well-defined contact area which can be obtained from the Hertz contact analysis. Within this contact region, some points may have different tangential velocities from the axis of rotation. This results in micro-slip between the contacting bodies within the contact area, and the effect will be a maximum at the edges of the contact area, also called Heathcote slip (ξ). Micro-slip was thus analysed at the edges of the major axis of contact area (a). The micro-slip for any point within the contact area due to contact conformity can be expressed as the 'Heathcote' slip (ξ):

$$\xi(y) = \frac{(\gamma b)^2 - y^2}{2R^2} \quad (10)$$

where R is the radius of the planetary ball, b is the contact width in the transverse direction, and $y = \gamma b$ is the position

Table 1
Effect of micro-slip with contact stress

Peak compressive stress (Po) (GPa)	Contact width (*b*) (mm)	Micro-slip (% sliding)
2	0.17	− 3
2.3	0.20	− 4
2.7	0.23	− 6

of the lines of no slip. The contact is made up of regions of stick and positive/negative slip. Variable γ is the location of the pure rolling region and is determined using defined equations [16]. The evaluation of this variable requires an iterative technique. When friction is low and the degree of oscillation is high, a simplified approach can thus be used to determine γ. It is assumed that complete slip occurs at all points off the pure rolling lines and that there is no net tangential force. This yields a value of $\gamma = 0.35$. Table 1 shows the effect of Hertzian contact stress on the %sliding of maximum slip within the contact region.

3. Experimental test results

Rolling contact fatigue (RCF) tests were conducted under different tribological conditions of Hertzian contact stress and contact configuration. Table 2 displays the conditions for each test, while RCF test results are shown in Fig. 2. These results are not intended for statistical fatigue life prediction, but to understand the performance of the coated specimens in RCF tests under various HIPing conditions. The Peak compressive stress values listed in Table 2 were based upon the uncoated case of the contacting rolling elements, hence giving a more conservative comparison, however, it should be noted that the compressive stress in the post-treated coatings was higher (to what is shown in Table 2), due to the increase in coating's indentation modulus after the post-treatment. Maximum tensile stress values listed in Table 2 were however based on the experimental measurements of indentation modulus.

3.1. Surface observations

Fig. 3 displays the surface observation of failed coatings tested at a contact stress of 2 GPa. Fig. 3(a) shows the surface observation of the as-sprayed WC–NiCr failed coated disc (T1). Surface failure was in the form of a spall, which, initiated in the wear track. At HIPing temperatures of 1200 °C, no failure occurred on the wear track of the coated disc (T9) as shown in Fig. 3(b). Contact stress remained constant at 2 GPa and the lower planetary balls were steel. The width of the wear track was measured as 400 μm. This compares well with the theoretical values displayed in Table 2.

Fig. 4 shows the surface observations of the failed coated discs tested under identical tribological conditions and at a higher Hertzian contact stress of 2.3 GPa. Fig. 4(a) displays the surface observation of an as-sprayed failed coated disc. Within the area of failure, a dent is observed.

Table 2
Rolling contact fatigue tests for as-prayed, HIPing at 850 °C, HIPing at 1200 °C and vacuum-heated HVOF coated rolling elements on bearing steel (440-C) substrate

Test no.	Contact load (F) (N)	Planetary balls	Contact stress (Po) (GPa)	Contact width (mm)	Depth of maximum shear stress (μm)	Depth of orthogonal shear stress (μm)	Max tensile stress (MPa)	Test lubricant	Failure type
As-sprayed tests									
T1	130	Steel	2	0.35	84	62	272	Vitrea 320	Spalling
T2	190	Steel	2.3	0.4	97	71	311	Vitrea 320	Spalling
T3	310	Steel	2.7	0.47	114	83	365	Vitrea 320	Delamination
T4	220	Ceramic	2.7	0.39	95	70	368	Vitrea 320	Delamination
HIPed at 850 °C tests									
T5	130	Steel	2	0.35	84	62	311	Vitrea 320	Spalling
T6	190	Steel	2.3	0.4	97	71	352	Vitrea 320	Delamination
T7	310	Steel	2.7	0.47	114	83	369	Vitrea 320	Delamination
T8	220	Ceramic	2.7	0.39	95	70	428	Vitrea 320	Delamination
HIPed at 1200 °C tests									
T9	130	Steel	2	0.35	84	62	324	Vitrea 320	None[a]
T10	190	Steel	2.3	0.4	97	71	367	Vitrea 320	Spalling
T11	310	Steel	2.7	0.47	114	83	385	Vitrea 320	Delamination
T12	220	Ceramic	2.7	0.39	95	70	451	Vitrea 320	Delamination
Vacuum-heated tests									
T13	130	Steel	2	0.35	84	62	345	Vitrea 320	Surface distress
T14	310	Steel	2.7	0.47	114	83	460	Vitrea 320	Surface distress
T15	220	Ceramic	2.7	0.39	95	70	487	Vitrea 320	Surface distress

[a] Suspended test after 70 million stress cycles.

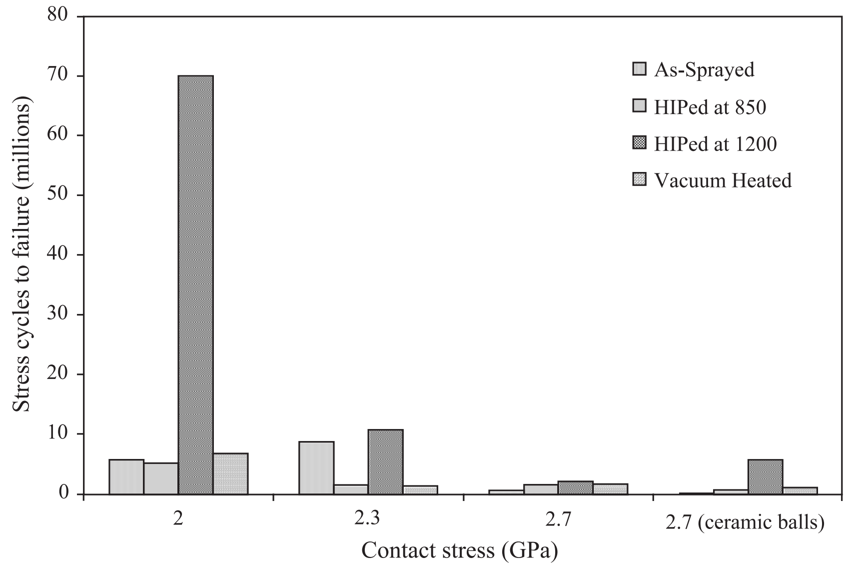

Fig. 2. Rolling contact fatigue test results for as-sprayed, HIPing at 850 °C, HIPing at 1200 °C and vacuum-heated HVOF coated rolling elements.

The formation of a dent may have triggered from initial debris from a spall. Abrasive wear from the dent and evidence of micro-cracking leading to debris about to detach from the coating were also observed. Fig. 4(b) displays the surface observation of a failed post-treated coated disc (T6). HIPing at 850 °C led to the formation of identifiable cracks within the wear track which triggered the vibration sensor after 3 million stress cycles. Fig. 4(c,d) displays the surface observation of a failed coated disc HIPed at 1200 °C (T10). Observation of Fig. 4(d) indicates that failure is in the form of a relatively deep spall (Table 3). Debris from the spall has led to a crown of micro-pits which has widened the wear track since Table 2 indicates a contact width of 400 μm.

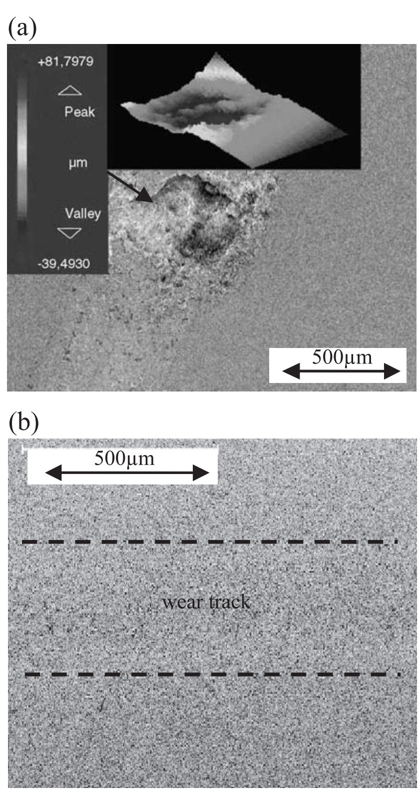

Fig. 3. Surface observations for WC–NiCr coatings tested at 2-GPa contact stress (test T1, T9): (a) as-sprayed coating (test T1); (b) HIPed at 1200 °C coating (test T9). 3D Interferometric image also shown on (a) to display depth of failure listed in Table 3 for Test T1.

Fig. 5 displays the surface observations for as-sprayed and post-treated coatings subjected to a contact stress of 2.7 GPa using steel planetary balls. Fig. 5(a) shows the surface observation of an as-sprayed failed coated disc (T3). Delamination is observed within the wear track. Observation of the HIPed at 850 °C coated disc (T7) in Fig. 5(b) displays evidence of coating delamination. Delamination differs from spalling failure in that the pit is normally deeper, greater in magnitude and hence, spreads out with the wear track. Surface observation of the failed coated disc HIPed at 1200 °C (T11) in Fig. 5(c) displayed similar failure to disc (T7) in Fig. 5(b) in that significant coating delamination triggered test termination. Fig. 5(d) shows the surface observation of a failed vacuum-heated coated disc (T14). The observation of surface distress within the wear track was initiated by a high frequency of micro-cracks at the edge of the contact region. Propagation of the cracks led to debris entrapment within the wear track.

Fig. 6 shows the surface observations for coatings subjected to a contact stress of 2.7 GPa using ceramic balls. Fig. 6(a) shows the surface observation of a failed as-sprayed-coated disc (T4). Mode of failure was identified as delamination. Fig. 6(b) shows the surface observation for a failed coated disc HIPed at 850 °C (T8). Significant coating delamination is identified as the mode of failure. Fig. 6(c)

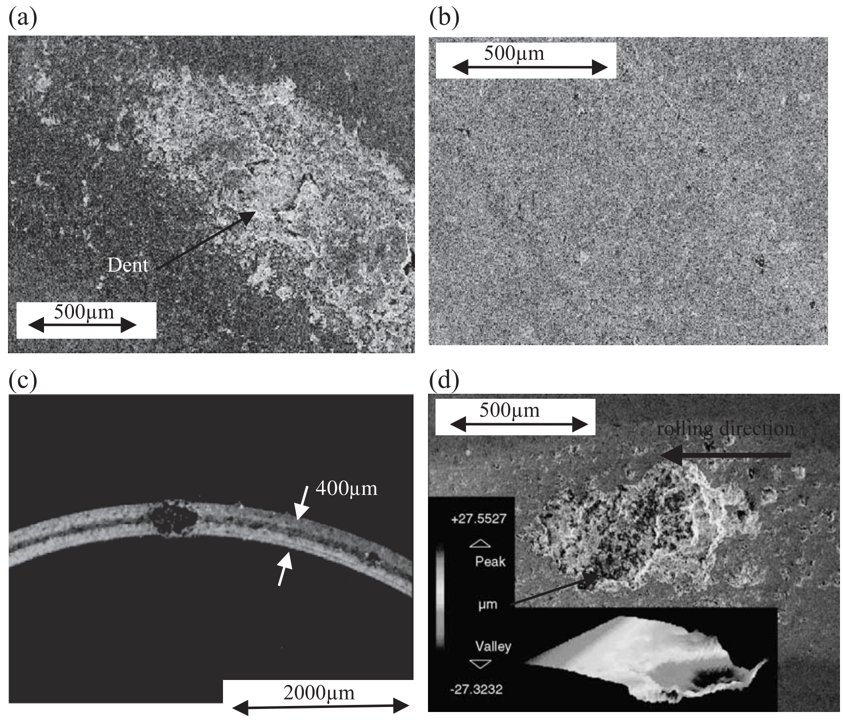

Fig. 4. Surface observations for WC–NiCr coatings tested at 2.3-GPa contact stress (tests T2, T6, T10): (a) as-sprayed coating (T2); (b) HIPed at 850 °C coating (T6); (c) light microscope image of HIPed at 1200 °C coating (T10); (d) SEM image of HIPed at 1200 °C coating (T10). 3D interferometric image included in (d) to show depth of failure listed in Table 3 for test T10.

shows the surface observation for a failed coated disc HIPed at 1200 °C (T12). Large sheet-like debris has delaminated from the wear track and micro-cracks are observed at the edge of the contact region. In Fig. 6(d), micro-cracks are observed which terminated the test for a vacuum-heated coated disc (T15).

3.2. Microstructural observations

The microstructure of the as-sprayed and post-treated coatings was observed using Back Scattered and Secondary Electron Imaging. Fig. 7 shows the observations of an as-sprayed WC–NiCr functional graded coating. Fig. 7(a) shows the overall view of the coating microstructure. Fig. 7(b) shows a detailed image of the upper layer. The lower layer is displayed in greater detail in Fig. 7(c). Fig. 7(d) shows the interface between the coating and substrate at high magnification.

Table 3
Depth measurements for failures on as-sprayed, HIPed at 850 °C, HIPed at 1200 °C, and vacuum-heated failed coated discs

Test no.	Depth of max shear Stress (μm)	Depth of orthogonal shear stress (μm)	Depth of failure (μm)
T1	84	62	48
T3	114	83	84
T4	95	70	33
T7	114	83	66
T8	95	70	59
T10	97	71	55
T11	114	83	63
T12	95	70	56
T13	84	62	30
T14	97	71	70
T15	114	83	7

Fig. 8 shows the cross-sectional observations of a coating HIPed at 850 °C. Fig. 8(a) shows the overall view of the coating microstructure. Fig. 8(b) shows the microstructure of the upper layer at high magnification. The lower layer is shown in greater detail in Fig. 8(c). Fig. 8(d) shows the interface between the coating and substrate at high magnification.

Fig. 9 shows the observations of a coating HIPed at the elevated temperature of 1200 °C. Fig. 9(a) shows the coating/substrate interface at relatively low magnification. Fig. 9(b) shows the microstructure of the upper layer in detail. Fig. 9(c) shows the microstructure of the lower layer at high magnification. The interface between the two layers at high magnification is shown in Fig. 9(d).

Fig. 10 shows the observations of a coating vacuum heated at 1200 °C. Fig. 10(a) shows the coating/substrate interface at relatively low magnification. Fig. 10(b) shows the lower layer at high magnification.

3.3. Depth analysis of coating failures

Depth analysis of the areas of failure on the wear tracks of the tested coatings enabled further insight into the origin of failure initiation. Measurements were taken using a

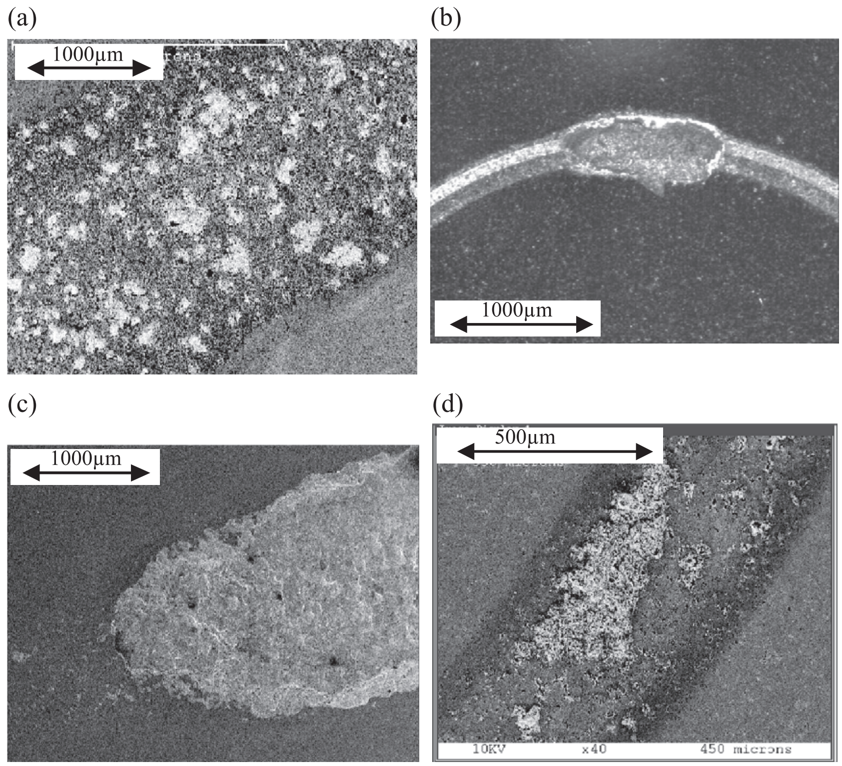

Fig. 5. Surface observations for WC–NiCr coatings tested at 2.7-GPa contact stress (tests T3, T7, T11, T14): (a) as-sprayed coating (T3); (b) HIPed at 850 °C coating (test T7); (c) HIPed at 1200 °C coating (T11): (d) vacuum-heated coating (T14).

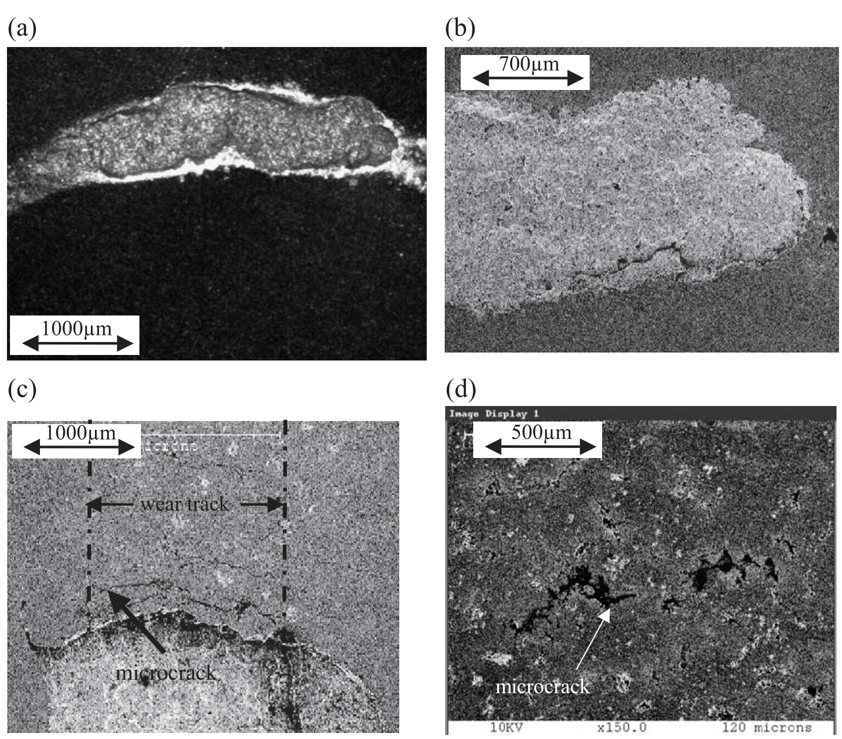

Fig. 6. Surface observations for WC–NiCr coatings tested at 2.7-GPa contact stress using ceramic planetary balls (tests T4, T8, T12, T15): (a) as-sprayed coating (T4); (b) HIPed at 850 °C coating (T8); (c) HIPed at 1200 °C coating (T12); (d) vacuum-heated coating (T15).

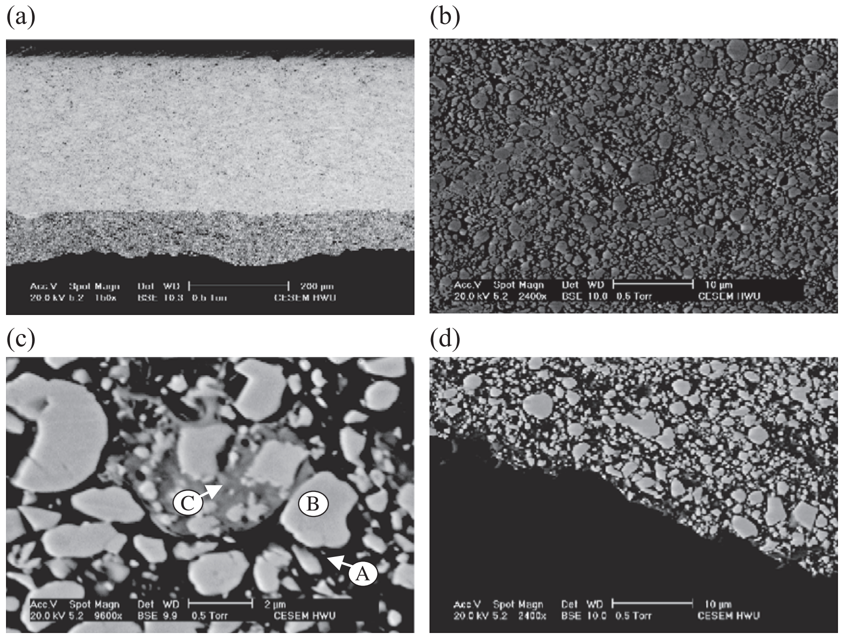

Fig. 7. Microstructure observations for as-sprayed WC–NiCr coating: (a) coating; (b) upper layer of FGM; (c) lower layer of FGM; (d) coating/substrate interface.

scanning white light Interferometer. Previous investigations have attributed sub-surface failure to the location of either maximum shear or orthogonal shear stress. Hence, in Table 3, depths of failure and location of maximum shear and orthogonal shear stress are listed for a number of tests. Typical examples of the 3D interferometric images of the failures used to ascertain the depth values in Table 3 can also be seen in Figs. 3(a) and 4(d) for Tests T1 and T10, respectively.

3.4. Micro-hardness and indentation modulus analysis

Hardness and indentation modulus measurements were performed on the as-sprayed and post-treated thermal spray coatings. Indentation modulus values were obtained using a nano-indentation system.

Micro-hardness and the indentation modulus measurements were taken on the surface and cross-section of as-sprayed, HIPed at 850 °C, HIPed at 1200 °C and vacuum-

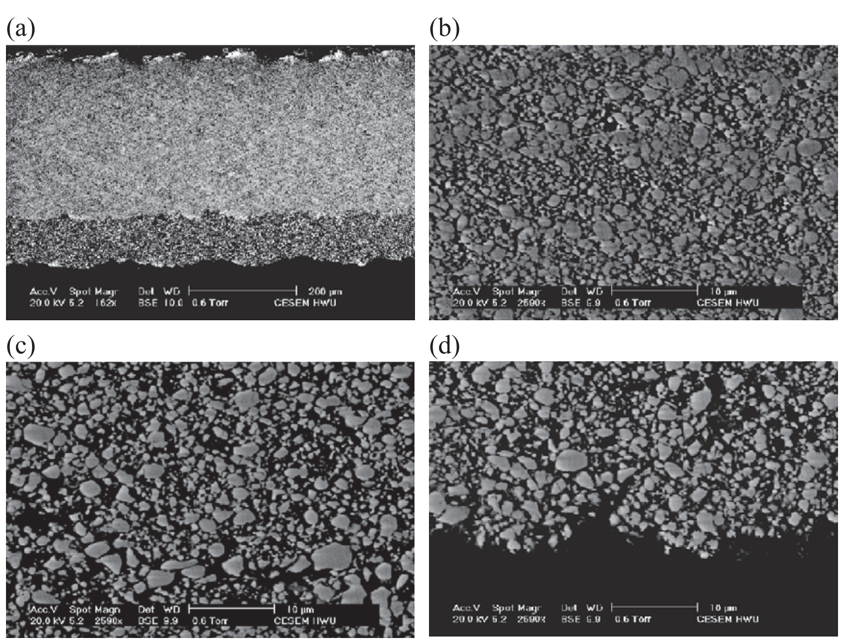

Fig. 8. Microstructure observations for HIPed at 850 °C WC–NiCr coating: (a) coating; (b) upper layer of FGM; (c) lower layer of FGM; (d) coating/substrate interface.

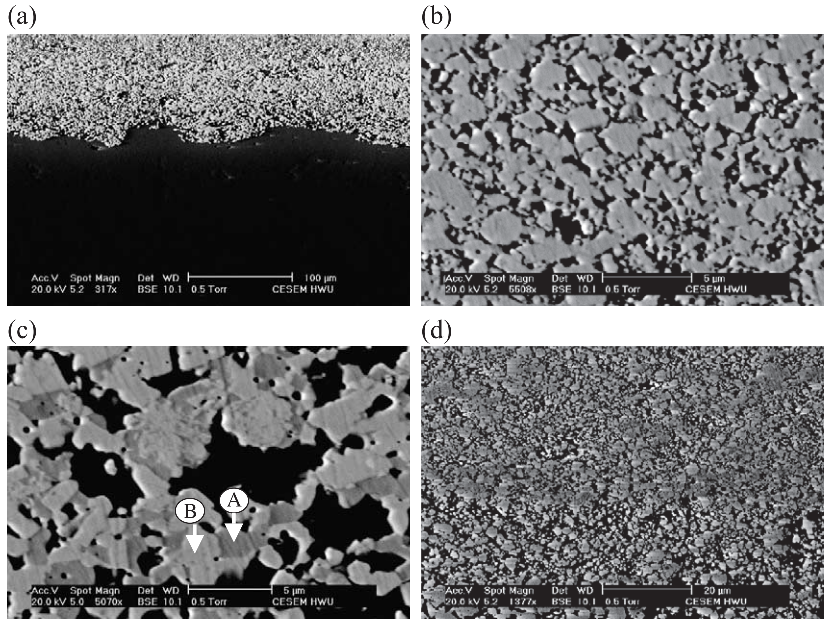

Fig. 9. Microstructure observations for HIPed at 1200 °C WC–NiCr coating: (a) coating; (b) upper layer of FGM; (c) lower layer of FGM; (d) lower layer/upper layer interface.

heated discs. Hardness measurements were taken on the surface and on the cross-section of the coatings at a test load of 2.9N. Hardness results are displayed in Fig. 11(a). Results from the as-sprayed coating show a surface hardness of 845 HV. In comparison, results from the surface of the coating HIPed at 850 °C display a slight increase in hardness of 965 HV. Increasing the HIPing temperature to 1200 °C led to an increased surface coating hardness of 1189 HV. The vacuum-treated coating had an average surface hardness of 1206 HV.

Hardness measurements taken on the cross-section indicated similar trends as observed in the surface hardness values, however, indentations made on the lower layer of the FGM yielded some unusual results. As-sprayed coatings showed a hardness of 1060 HV at 350 μm. Coating HIPed at 850 °C showed a lower hardness of 862 HV at this depth. HIPed at 1200 °C and vacuum-treated coatings displayed similar hardness values at this depth of 783 and 729 HV, respectively.

Indentation Modulus results are shown in Fig. 11(b). Measurements were taken on both the surface and cross-section at a test load of 500 mN. Results from the surface of the as-sprayed coating displayed an average value of 250 GPa. Results from the surface of the coating HIPed at 850 °C displayed a slightly higher value of 300 GPa. On increasing the HIPing temperature to 1200 °C, a slight increase in the indentation modulus was observed from surface measurements. However, the surface value for the vacuum-heated coating was 500 GPa which was significantly higher than all other coatings. Indentation modulus results on the cross-section of the coating within the upper layer of the FGM were observed to be higher in the HIPed coatings. Indentation modulus results for the as-sprayed coating remained constant at 185 GPa through out the upper layer. Results for the vacuum-heated coating dropped in moving away from the surface and at a depth of 250 μm also displayed an average value of 185 GPa. In comparison, HIPed coatings displayed significantly higher values at this depth.

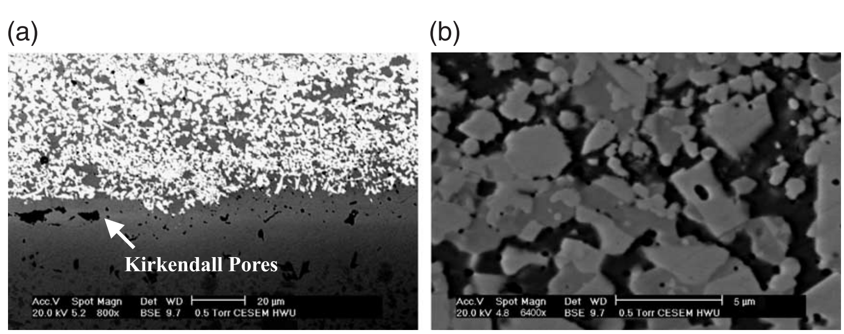

Fig. 10. Microstructure observations for vacuum-heated WC–NiCr coating: (a) coating; (b) lower layer of FGM.

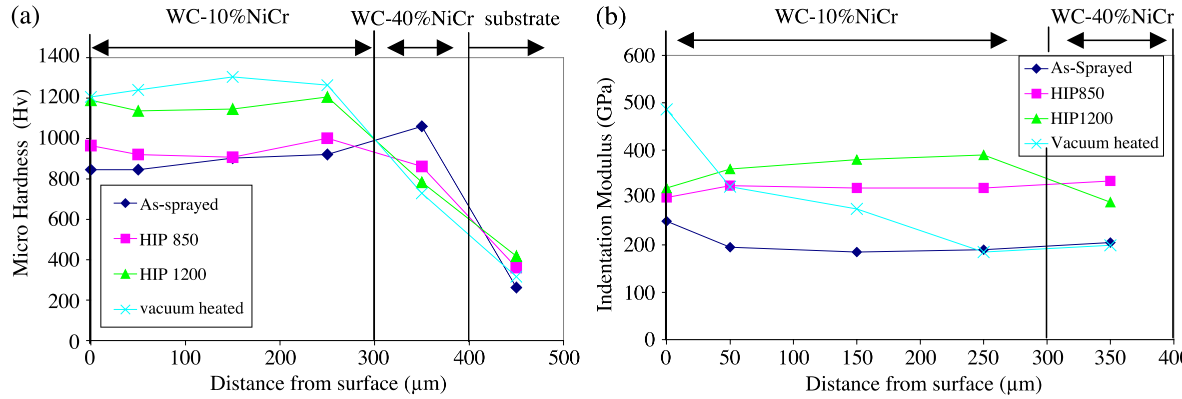

Fig. 11. Microstructural analysis of coatings. (a) Micro-hardness results for as-sprayed, HIPed at 850 °C, HIPed at 1200 °C, vacuum-heated Coatings; (b) indentation modulus results for as-sprayed, HIPed at 850 °C, HIPed at 1200 °C, vacuum-heated coatings.

3.5. X-ray diffraction

The coating was characterised through the use of a D500 X-ray diffractometer (XRD) operating at 40 kV and 20 mA with Cu Kα radiation (1.5406 Å, step size of 0.02° and dwell time of 2 s). The samples were run at 2θ from 20° to 100° to investigate the phase transformations that occurred during the coating deposition and post-treatment. XRD results for the WC–10%NiCr layer in both as-sprayed and post-treated coatings are presented in Fig. 12.

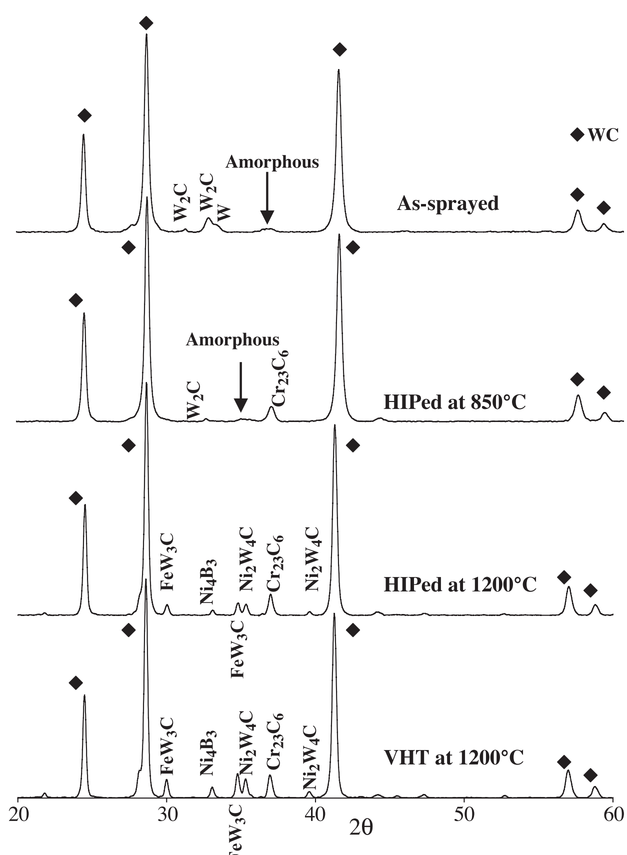

Fig. 12. XRD results for WC–10%NiCr (upper layer) for as-sprayed and post-treated coatings.

4. Discussion

4.1. Influence of coating microstructure

4.1.1. As-sprayed coatings

Fig. 12 shows the XRD spectrum of the upper layer of the as-sprayed coating. A broad amorphous hump was observed between 42° and 44° and two separate peaks identified as W_2C phases. The following reaction occurred during spraying:

$$2WC \rightarrow W_2C + C \quad (11)$$

$$W_2C \rightarrow 2W + C \quad (12)$$

Reactions (11) and (12) occur due to the decarburisation process which is kinetically driven and has been well documented in previous investigations on Thermal Spraying [17]. The degree of decarburisation is related to the manufacturing process of the powder, the deposition process flame temperature and flame velocity. The lower flame temperature experienced in the HVOF flame results in less reactions in the carbide particles during spraying, though some decomposition occurs as the use of agglomerated and sintered powders leads to a higher degree of carbide dissolution [18]. Fig. 7 shows the microstructure of the as-sprayed coating. In both the upper and lower layers of the FGM, two distinct matrix and carbide types were observed. The matrix marked (A) is very dark indicating a low mean atomic number. The carbide grains within it were of an angular and blocky morphology (marked (B)), therefore, no evidence of carbide dissolution. The second type of matrix observed (marked (C)) was much brighter (indicating a higher mean atomic number) and the carbides which it encapsulated were smaller, rounder and had a brighter rim. The rim of second phase material was identified as W_2C. In this region, the carbides have dissoluted in the liquid NiCr during spraying forming Ni_2W_4C (amorphous hump). The surrounding matrix was enriched in both carbon and tungsten (leading to its brighter contrast in the back scattered electron image) and leaving a rim of W_2C surrounding the WC particle. The regions in the coating which showed greater reactions between the binder and the carbide were at the outer regions of the original carbides where higher temperatures were experienced during spraying. It is interesting to note that in previous investigations [8], cracking has been seen in the region of the binder enriched with tungsten and carbon, although not seen in this investigation due to the magnification limit of Back Scattered Electron imaging. This indicates that this phase was brittle which could lead to poor RCF performance.

The change in microstructure between the upper and lower layer of the FGM resulted in slightly different mechanical properties as shown in Fig. 11. The microhardness of the lower layer was slightly higher than the values obtained for the upper layer. Although not reported in this investigation, a number of crystalline phases were observed in the XRD pattern of the lower layer ($Cr_{23}C_6$, Ni_2C_x), which were not observed in the upper layer XRD spectrum as shown in Fig. 12. The combination of these crystalline phases and an increased percentage of matrix (40%NiCr) within the lower layer led to increased binder strength as a result of alloying during spraying.

4.1.2. HIPed at 850 °C coatings

The microstructure of the upper layer of the HIPed at 850 °C coating was similar to the microstructure of the as-sprayed coating, however, the XRD pattern indicated a reduction in the intensity of the amorphous phase as well as the formation of a new peak identified as $Cr_{23}C_6$. DTA analysis of WC coatings indicated an exothermic reaction occurs at about 831 °C [17]. At this temperature, the amorphous phase starts to crystallise to form complex carbides with the precipitation of free carbon. The lack of tungsten in the XRD spectrum suggests the tungsten and carbon were consumed by Ni solid solution to form the intermetallic complex carbide Ni_2W_4C, which was too low in intensity to be observed in the XRD spectrum at this post-treatment temperature. Since the amorphous hump was still observed, it is likely this will have an adverse effect on the RCF performance.

The mechanical properties of the coating changed with HIPing at 850 °C. Dissolution of carbides resulted in solid state sintering and the formation of physical bonds between the mechanically interlocked splats, hence, the values for elastic modulus increased with HIPing and in particular the value for the upper layer was higher than the lower layer. Due to the complexity of the coating microstructure, a number of hardness mechanisms were responsible for the changes in hardness with HIPing at 850 °C. For WC cermets, the model of Lee and Gurland [19,20] has been commonly applied.

$$H_C = H_{WC} V_{WC} C + H_M (1 - V_{WC} C) \tag{13}$$

The cermet hardness (H_C) is based on the hardness and volume fraction of the hard phase (H_{WC} and V_{WC}) and the hardness of the matrix phase (H_M). The contiguity (C) defined by Gurland describes the percentage surface area of a carbide grain in contact with other carbide grains and accounts for the microstructural influence of the carbide morphology. The hardness of the two phases is microstructure dependant. Carbide hardness is a function of grain size, smaller grains giving higher hardness values. With regard to the overall cermet hardness, higher degrees of contiguity generates harder material. In addition, for thermally sprayed cermet coatings, splat to splat bonding will also affect the overall hardness. In the lower layer, recovery, recyrstallisation and grain growth occur rapidly, reducing the dislocation density, increasing the grain size and relieving any internal stresses within the splats. These transformations lead to matrix phase softening and account for the reduction in hardness which is observed in Fig. 11. Within the upper layer, the reduction in binder led to a higher percentage of dissolved tungsten and free carbon within the binder which inhibited dislocations motion [21]. The structural disorder caused by the higher percentage of dissolved W and C was observed in the larger XRD peak widths for the matrix phase in the upper layer. The extent of binder phase was dependant on the deposition parameters being more influential in the higher temperature techniques where extensive carbide dissolution meant that the upper layer acted more as a dispersion strengthened alloy than a carbide based composite.

4.1.3. HIPed at 1200 °C coatings

The microstructure of the coating changed significantly after HIPing at the elevated temperature of 1200 °C as shown in Fig. 9. In the upper layer, significant contact had occurred between the carbides and a number of micro-voids were observed in the centre of the carbides. Similar characteristics were observed in the lower layer, however, in addition the carbides were slightly darker at the boundaries with the binder and an inter-diffusion layer was observed at the coating/substrate interface. The XRD pattern showed that the amorphous hump had disappeared and a number of new narrow peaks were visible. The new peaks were identified as complex carbides (Ni_2W_4C, FeW_3C). The W_2C peak was also no longer visible.

At elevated temperatures the reaction ($4WC + 2Ni \rightarrow Ni_2W_4C + 3C$) and reaction ($3WC + 3Fe \rightarrow FeW_3C + 2C$) take place during the recrystallization of the amorphous phase and form eta carbides. The enriched tungsten and carbon which existed within the amorphous phase was consumed by Ni and Fe. Dissolution of the WC carbides and formation of FeW_3C also resulted in free carbon to assist the formation of complex chromium carbides such as $Cr_{23}C_6$ seen in the XRD spectrum. Fig. 9(c) shows two different carbides within the matrix. The darker carbide has formed from recrystallization of the amorphous region and also dissolution of WC in nickel matrix. EDX analysis of this region showed a high percentage of nickel and tungsten but a relatively low percentage of chromium within this region which suggests evidence of a nickel-based carbide (Ni_2W_4C). Chromium carbides were forming elsewhere in the microstructure from carbide dissolution. The diffusion layer observed at the coating/substrate interface has been observed in previous investigations on the post-treatment of WC–NiCr coatings and EPMA analysis showed that this interfacial layer contained predominantly nickel, though chromium and iron were also observed. Carbon and tungsten were not observed since they had dissolved in the matrix to form complex carbides. The formation of a diffusion layer is the result of the Kirkendall effect and is the end result of two chemical species (Ni and Fe) diffusing in opposite directions at different rates [4]. Proof of the Kirkendall effect is verified by Kirkendall pores in either the coating next to the diffusion layer or at substrate, however, unlikely to be seen in the coatings as they were reduced in size due to compaction during HIPing. Nickel is the dominant species in the diffusion layer because nickel diffuses from the coating across the diffusion layer into the substrate more rapidly than iron in the opposite direction, leading to unequal fluxes of the two species from different directions (Kirkendall effect). A net diffusional mass flows from the coating to the substrate representing the diffusion layer growing by consuming the coating. As the diffusion layer moves towards the substrate, an excess of vacancies which later become pores (Kirkendall pores) form in the coating neighbouring the diffusion layer. As the diffusion layer moves towards the coating, the Kirkendall pores become part of the diffusion layer. When the coating is subjected to HIP treatment, the Kirkendall pores can be partially closed up or reduced in size due to compaction which increases the contact area between the coating and the diffusion layer and thus speeds up element diffusion and transition layer growth.

The mechanical properties were significantly influenced by the changes within the coating microstructure. The hardness of the upper and lower layers was similar to the coating HIPed at 850 °C, therefore, it is likely that the hardness mechanisms occurring at 850 °C were still occurring at 1200 °C. The increase in carbide dissolution and necking between the carbides led to higher elastic modulus values.

4.1.4. Vacuum-heated coatings

The microstructure of the coating vacuum heated at 1200 °C was similar to HIPed at 1200 °C microstructure as shown in Fig. 10. However, a number of pores were observed within the diffusion layer, which were identified as Kirkendall pores. During HIPing at 1200 °C, these pores were closed up, however, due to the absence of high isostatic pressure in vacuum heating, the pores did not reduce in size. The XRD pattern was also similar, however, the narrow complex carbide peaks were slightly higher in intensity. A noticeable difference was observed in the mechanical properties of the two coatings as seen in Fig. 11(a,b). The hardness value for the upper layer was slightly higher than the value for the upper layer of the HIPed at 1200 °C coating, however, the hardness values for the lower layer were similar. The elastic modulus of the vacuum-heated coating significantly reduced with coating depth. This trend was not observed in the HIPed coatings. The increase in elastic modulus in the HIPed coatings is attributed to both carbide dissolution and necking between the carbides. Dissolution of carbides occurs at high temperatures and is not pressure dependant. The formation of chromium carbides and other phases has been observed in previous investigations on the heat treatment of WC cermet thermal spray coatings [22,23]. However, the process of necking is localised to the post-treatment, HIPing. The process of densification within the powder during HIPing at elevated temperatures is a two-step process [24]. Initially, neck growth occurs at the contacts between the carbides. At this stage, the carbides are beginning to bond but the porosity is still interconnected. The mechanism of the phenomena of neck growth is determined as grain boundary diffusion creep. With eventual final densification, the material is considered a solid containing isolated pores. Therefore, the absence of neck growth in the vacuum-heated coating microstructure led to low levels of elastic modulus as observed in Fig. 11(b) which is detrimental to improvement in RCF performance.

4.2. RCF failure modes

Classification of failure modes was made on the basis of surface and sub-surface observations of the failed rolling elements. Since the modified four-ball machine runs at high speed, it is difficult to observe crack propagation. Post-test examination is the only method to ascertain failure modes and mechanisms. A principal aim of the current study was to ascertain whether similar failure modes occurred in post-treated coatings as had been previously seen in as-sprayed thermal spray coatings. Classification of failure modes in thermal spray coatings has been previously categorised into four main modes and named as abrasion, delamination, bulk failure and spalling [25]. However, as seen in Table 2, only three modes of failure were identified in post-testing analysis. They were delamination, spalling and surface distress.

4.2.1. Delamination in RCF failure

Suh initially proposed the delamination theory of sliding wear in 1973. Suh [26], Flemming and Suh [27], Suh and Saka [28] and Suh [29] have since performed experimental and theoretical analysis supporting the delamination theory. The mechanism of delamination wear includes the propagation of cracks parallel to the surface at a depth governed by material properties and friction coefficient. Although rolling friction prevails in modified four-ball tests and delamination theory is based on sliding friction, the results are still compelling. Damage theory of materials begins with the premise that material contains a multitude of defects in the form of micro-voids [25] which undergo extension due to loading and unloading. A similar approach is adapted to explain the mechanism of coating delamination. The coating microstructure contains varying levels of micro-pores, micro-cracks and secondary phase particles, which act as stress concentration points during cyclic loading. A typical example of delamination failure on the wear track can be seen in Figs. 5(a,b) and 6(b,c) for the as-sprayed and post-treated coatings.

4.2.2. Spalling in RCF failure

Spalling is the most commonly seen failure in conventional steel rolling element bearings. Spalling fatigue, however, is the rarest mode of failure in thermal spray coatings. Tallian [25] defined a spall as a sharp edged bottom feature formed by the fracture of a surface. Spall in thermal spray coatings resembles in appearance to the spalls in conventional bearings and differs from delamination failure. The spall is contained within the wear track and it is circular or elliptical in appearance with its surface area (width to depth ratio) much smaller than that of a delaminated coating as shown in Fig. 4(c). Spalls can initiate from micro-pits, furrows, grinding marks or dents on the surface of a wear track. In addition, sub-surface inclusions and defects are known to lead to spalling of rolling elements.

4.2.3. Surface distress in RCF failure

Surface distress is defined as micro-scale spalling fatigue. It is the failure of rolling contact surfaces resulting in asperity scale micro-spall craters. Surface distress has been reported predominantly on steel rolling contact surfaces. However, silicon nitride ceramic components also exhibit the micro-cracking and micro-spalling features of surface distress. The theory of surface distress in metal is discussed in detail by both Tallian [25] and Suh [26]. Both define the failure process as a mechanism of asperity contact in the presence of micro-slip and sliding which is responsible for micropitting and sliding wear. Under full film EHL test conditions, surface distress does not occur because the film prevents high micro-stresses in asperity interactions. However, if the formation of a spall or micro-pit from delamination does not trigger the vibration sensor during RCF testing, the debris from the damaged area can enter the contact area, which disrupts the EHL film. The damage to the coating surface in this case is controlled by the size of the debris. The size of the debris is related to the critical crack size in the contact stress field, and hence, a particle cannot be crushed below this threshold. The difference in hardness between the coating and the planetary balls also has a significant effect on the material removal process. The contact is subject to micro-slip (Table 1) so within the contact, one surface moves with respect to the other, and hence, the trapped particle must accommodate this slip. As well as the mechanism of asperity deformation leading to micropitting of the surface, the criterion of maximum tensile stress at the edge of the contact area for brittle materials also needs to be considered. Stresses are sharply localised and decay rapidly at relatively low depths below the surface. Tucker [30] showed that the fracture stress of WC–Co coatings using the technique of tensile test, free standing ring is in the range of 380–690 MPa for HVPS and D-Gun coatings. The combination of high micro-hardness and the steep gradient in indentation modulus values for vacuum-heated thermal spray coatings can result in low levels of fracture stress. Hence tensile stress at the edge of the contact region under Hertzian stresses will be similar to the fracture stress. This indicates that even under the fully developed EHL regime, micro-cracks can propagate because of tensile stressing at the edge of the contact area. Figs. 5(d) and 6(d) show the SEM observation of surface distress in as-sprayed and post-treated coatings.

4.3. Effect of contact stress on RCF failure modes of as-sprayed and post-treated WC–NiCrBSi coatings

4.3.1. As-sprayed coatings

In general, the RCF performance of as-sprayed coatings decreased with increase in Hertzian contact stress. Test T1 was performed at stress levels of 2 GPa. Failure was identified in both tests as formation of a spall within the wear track as shown in Fig. 3(a). Spalls can initiate from surface and sub-surface defects. All tests were conducted under full film EHL, therefore, the spall did not initiate from asperity contact. The initiation of cracks during rolling contact was unlikely due to the relatively low levels of maximum tensile stress (Table 2) and low contact pair hardness since tests were conducted using steel planetary balls. The mechanism of sub-surface spalling is attributed to the formation of micro-cracks which initiate from defects which are located near but in general above the depth of maximum shear stress [25]. The depth of orthogonal shear stress under Hertzian contact is located above the depth of maximum shear stress and is evaluated using conventional contact mechanics approach [13]. Depth of spall observed on the wear track of test T1 was close to the location of orthogonal shear stress indicating failure was sub-surface initiated.

The RCF performance of T2 improved over T1 which was unusual since contact stress was increased in test T2 to 2.3 GPa. Failure in both cases was identified as sub-surface spalling. However, in test T2, the initial formation of the spall did not trigger the vibration sensor. Debris from the spall led to the formation of a dent as shown in Fig. 4(a). Denting is the result of an entrapped foreign body (debris) which is pressed into the contact surface during normal load and is most distinct on rolling surfaces where the relative motion in the contact is predominantly normal to the surface. The dent in Fig. 4(a) is surrounded by significant abrasive wear. Tallian discussed in certain circumstances that a dent may represent a sink for the EHL film in contact, which may locally depressurise the film, resulting in local film thinning around the dent edges. Asperity interactions occur which produces local surface distress. Hence, the formation of this secondary failure triggered the vibration sensor and terminated the test.

RCF performance in test T3 was less than both T1 and T2. The increase in contact stress to 2.7 GPa resulted in delamination failure on the wear track. In changing the steel planetary balls to ceramic balls, RCF performance reduced. A number of micro-cracks were observed at the edge of the contact region which was attributed to an increase in contact pair hardness. Delamination was observed on the wear track. Depth of failure was significantly less than the depth measured for test T3 as shown in Table 2.

The mechanism of failure for as-sprayed coatings was sub-surface initiated. During RCF testing, sub-surface failure initiates at either the location of maximum shear or orthogonal shear stress if defects exist within the coating microstructure. The amorphous regions in the as-sprayed coating are brittle and hence areas for crack initiation. The cracks initiating in these brittle regions would propagate during RCF testing due to the low value of elastic modulus leading to either delamination or spalling after relatively few stress cycles.

4.3.2. HIPed at 850 °C coatings

Coatings HIPed at 850 °C also displayed decreasing RCF performance with increasing contact stress. At 2-GPa contact stress, mode of failure was identified as surface distress. A dent is observed within the centre of the abrasive wear. Since the test was conducted in immersed lubricated conditions, the dent formed as a result of debris from the formation of an initial spall. Maximum tensile stress was evaluated as slightly higher than as-sprayed values due to the increase in levels of surface micro-hardness and indentation modulus, however, in the absence of any micro-cracking at the edges of the wear tracks, it is more likely the spall initiated from sub-surface defects. In increasing the contact stress to 2.7 GPa, the mode of failure changed to delamination, as shown in Fig. 5(b). Depth of failure was in the region of orthogonal shear stress. In changing the planetary balls from steel to ceramic, mode of failure was identified as delamination (Fig. 6(b)). Depth of failure was observed to be in the region of orthogonal shear stress. No micro-cracking was observed at the edges of the wear track, hence, mechanism of failure was sub-surface initiated.

The coatings HIPed at 850 °C therefore also failed from sub-surface defects. The analysis of the coating microstructure showed that the brittle amorphous region observed in the as-sprayed coating microstructure was still present after HIPing at 850 °C. Hence, the mechanism of failure did not change, which led to no improvement in RCF performance.

4.3.3. HIPed at 1200 °C coatings

No failure was observed on the wear track of the coating HIPed at 1200 °C and subjected to 2-GPa contact stress as shown in Fig. 3(b). The test was suspended after 70 million stress cycles. With increasing contact stress to 2.3 GPa, RCF performance reduced and failure was observed on the wear track. Fig. 4(c,d) shows the area of failure which formed on the wear track after 11 million stress cycles. Analysis of the failure shows a circular pit with a small width to depth ratio indicating mode of failure is spalling. Depth analysis of the failure area (Table 3) showed depth was only 55 μm. The 3D image of the failure area in Fig. 4(d) shows a pit with a flat bottom and a shallow entry angle wall which compares well with Tallian [25]. Spalling can initiate from both sub-surface and surface defects. Taillian classified the main difference between a sub-surface and surface spall by the angle of the entrance wall of the spall. A steep entrance wall indicates sub-surface spalling where as a shallow-angle entry wall is more characteristic of surface spalling. The spall was initiated from a surface defect, which gave rise to localised thinning of the EHL film and asperity interaction.

At the higher contact stress of 2.7 GPa, mode of failure changed to delamination (Fig. 5(c)). No micro-cracks were observed at the edge of the contact region. Depth analysis of the failure area listed in Table 3 indicated a depth of 62 μm which was significantly less than either orthogonal shear or maximum shear stress. Increase in contact stress requires the consideration of hydraulic pressure propagation proposed by Way [31]. In full film EHL Hertzian contact, lubricant can become trapped within a micro-crack which has initiated within the wear track. The high magnitude of contact stress pressurises the trapped lubricant which causes the crack to propagate deeper into the coating microstructure and hence result in sheet-like debris delaminating from the wear track. This led to sheet-like delamination.

In changing to ceramic planetary balls, mode of failure was identified as delamination as shown in Fig. 6(c). A number of cracks were also observed at the edges of the delamination. The formation of micro-cracks in full film EHL requires the consideration of the criterion of maximum tensile stress at the edge of the contact area. During rolling contact, micro-cracks would initiate and propagate which leads to either spalling or delamination depending on the hardness of the coating and influence of increasing contact pair hardness. Since micro-cracks were also observed at the edge of the contact region in tests conducted using ceramic balls on as-sprayed coatings, it is likely that the increase in contact hardness resulted in this failure in the HIPed at 1200 °C coatings.

The improvement in RCF performance was attributed to the significant changes in the coating microstructure with HIPing at the elevated temperature of 1200 °C. In the as-sprayed and HIPed at 850 °C coatings, the mechanism of failure was sub-surface initiated due to brittle amorphous regions in the microstructure which were determined areas of crack initiation. It was shown in Section 4.1.3. that the amorphous region completely recrystallised to form complex carbides at the elevated HIPing temperature of 1200 °C. The increase in elastic modulus indicated improved bonding between the splats which prevented crack-propagation. In addition, coatings heat treated at high temperatures have shown a reduction in residual tensile stresses and have attributed compressive stresses to the onset of cooling in which the substrate contracts more than the coating due to thermal mismatch which puts the coating into compression [17]. The compressive stresses prevent propagation of micro-cracks within the microstructure during rolling contact.

At higher stresses, failure occurred but mechanism and mode of failure were significantly different. Spalling was identified as the mode of failure in the disc HIPed at 1200 °C and subjected to 2.3 GPa, however, due to the significant improvement in coating microstructure, cracks did not initiate from sub-surface defects. At higher stress levels of 2.7 GPa, delamination was identified as the mode of failure. The effect of hydraulic pressure propagation (HPP) led to sheet-like debris delamination. With an increase in contact pair hardness, micro-cracks initiated at the edge of the contact region. The formation of complex carbides from recrystallised amorphous regions increased the hardness of the coating as they contain a high percentage of Tungsten. Hence, in the test conducted using ceramic balls, cracks initiated due to the increase in contact pair hardness and sliding within the contact region.

4.3.4. Vacuum-heated coatings

Vacuum-heated samples in general exhibited superior performance over as-sprayed and coatings HIPed at the lower temperature of 850 °C in RCF tests. At 2-GPa contact stress, failure was observed on the wear track in Fig. 3(d). A number of micro-cracks were observed at the edge of the contact region. Depth of failure is listed in Table 3 as 30 μm which was not close to the location orthogonal shear stress. Observation of the coating microstructure shown in Fig. 10(b) indicated a similar microstructure to HIPed at 1200 °C coatings as shown in Fig. 9(b). Indentation modulus results on the surface were significantly higher than any of the other coatings which dropped with increasing depth. The gradient indicated a lack of homogeneity which resulted in the coating exhibiting a brittle nature. Hence, the combination of brittle behaviour and maximum tensile stress led to initiation of micro-cracks at the edge of the contact region which gave rise to the formation of surface distress within the wear track.

With increasing contact stress, RCF performance lowered. Observation of values listed in Table 3 showed depth of failure increased with increasing contact stress in the tests conducted using steel planetary balls. This was attributed to the higher percentage of micro-slip and also the effect of HPP. Observation of the wear track on the failed coated disc, test T14, in Fig. 5(d) indicated no change in mode of failure.

In changing to ceramic balls, depth of failure decreased. Ceramic balls increased contact pair hardness. Failure initiated from micro-cracking at the edge of the contact region which propagated towards the centre of the wear track. The joining of cracks at the centre of the wear track led to debris delaminating and becoming entrapped during rolling contact. In tests conducted with the softer steel balls, initial debris entrapped within the wear track indented and became embedded within the planetary balls. In the tests conducted using the harder ceramic planetary balls, the initial debris deflected off the balls which resulted in increased vibration within the system and hence, triggered the vibration sensor. Therefore, less abrasive wear occurred before the test terminated.

Results from rolling contact fatigue tests conducted using vacuum-heated coated discs indicated improved performance over as-sprayed-coated discs. No failure initiated within the microstructure of the coating. High temperature alone improved the microstructure of the coating by recrystallisation of the brittle amorphous phase and elimination of tensile stresses. However, the exceptionally high value of indentation modulus measured on the surface of the coatings resulted in crack initiation at the edge of the contact region at all levels of contact stress. Propagation of micro-cracks led to significant surface distress. Therefore, the addition of high isostatic pressure during post-treatment of HVOF thermal spray coatings is critical to RCF performance. High isostatic pressure led to a more homogeneous coating as shown by the micro-hardness and indentation modulus results, and therefore, at low levels of contact stress, no cracks initiated at the edge of the contact region in coating HIPed at 1200 °C when subjected to 2 GPa contact stress.

5. RCF failures vs. functional graded coatings

In the series of RCF tests performed in the current investigation, contact stress was not raised above 2.7 GPa. Hence, depth of maximum shear stress was always located within the upper layer of the FGM. Analysis of the coating microstructure was therefore focused on the upper coating microstructure. This was based on the premise that the upper layer contains a higher percentage of tungsten carbide. Tungsten carbide provides inherent strength to the matrix, therefore, it was concluded that optimum performance in RCF testing would be observed within this range of contact stress.

Micro-hardness values for the lower layer in as-sprayed coatings were significantly higher than in the upper layer as shown in Fig. 11(a). This was attributed to the increase in amorphous phases in the lower layer due to the higher percentage of binder. Since W_2C is more brittle than WC, hardness of the lower layer was higher. The main objective of incorporating a lower layer within the coating was to reduce the transition in indentation properties, CTE mismatch strain and magnitude of residual stresses. Previous investigations on the RCF performance of HVOF thermal spray coatings by Ahmed et al. [14] have shown that poor adhesion at the coating/substrate interface led to delamination as a result of mismatch in indentation properties at the interface, quenching stresses and a contamination layer. The absence of adhesive failure in the fatigue evaluation of functionally graded coating highlights the inherent advantages multi-layer FGM coatings exhibit in the resistance to rolling contact fatigue.

6. Conclusions

1. HIPing at elevated temperatures of 1200 °C resulted in significant improvement in RCF performance at low levels of contact stress. No failure occurred at 2-GPa contact stress. Improvement was attributed to significant improvement in the coating microstructure with recrystallisation of the amorphous phase, formation of complex carbides and improved bonding between the splats preventing failure at low levels of contact stress. At higher levels of contact stress, the combination of increase in maximum tensile stress, contact pair hardness (ceramic balls) and influence of hydraulic pressure propagation resulted in failure by surface delamination.
2. Coatings vacuum-heated at 1200 °C displayed improved performance in RCF testing at all levels of contact stress over as-sprayed coatings. This post-treatment gave rise to dissolution of carbides. However, the absence of homogeneous behaviour led to failure at all levels of contact stress. Micro-cracks initiated at the edge of the contact region during rolling contact which propagated and gave rise to significant surface distress. The initiation of micro-cracks was attributed to levels of maximum tensile stress evaluated from extremely high indentation modulus values measured on the surface, which exceeded the fracture stress of the coating.
3. Coatings HIPed at 850 °C showed no improvement in performance over the as-sprayed coatings in RCF testing. Mode and mechanism of failure was identified as sub-surface delamination which remained consistent at all levels of contact stress. Evidence of an amorphous phase which is brittle in nature was identified as the probable location of crack initiation during RCF testing. Due to low levels of elastic modulus, cracks propagated towards the surface.
4. The functional graded thermal spray coating failed at all levels of contact stress from sub-surface delamination which was attributed to the formation of an amorphous phase, which formed during spraying. Comparison of test results with previous RCF investigations on HVOF thermal spray coatings of the same thickness and under similar conditions showed that functional graded thermal spray coatings exhibited improved performance. This was attributed to the improved bonding at the coating/substrate interface as no adhesive failure occurred.

Nomenclature

N	Speed of the drive shaft (rpm)
R_a	Radius of the coated disc (mm)
R_p	Radius of the lower planetary ball (mm)
R_2	Radius of the upper wear track on the drive disc (mm)
R_i	External radius of the cup (mm)
R_c	Radius of the cup (mm)
ω_a	Angular velocity of the upper drive disc about the spindle axis MN
ω_p	Angular velocity of the planetary ball about the axis MN
ω_s	Spin angular velocity of the planetary ball about the axis inclined at angle β to the spindle axis MN
θ	Angle between the axis of the driving shaft and the connecting line of centres of the driver plate and the driven ball
β	Angle between the axis of the driving shaft and the axis of spin of the planetary balls
δ	Angle between the spin axis of rotation of the planetary ball and the connecting line of the conjunctions formed between the planetary balls and the cup
Z	Number of planetary balls

Acknowledgements

The authors would like to thank Dr. Susan Davies at Bodycote Hot Isostatic Pressing/Infutec for the post-treatment of thermal spray coatings, and also Professor Rainer Gadow at the University of Stuttgart for the indentation modulus measurements. The authors also acknowledge the financial support of EPSRC (GR/R45284) to fund this project.

References

[1] A. Nakajima, T. Mawatari, M. Yoshida, K. Tani, A. Nakahira, Wear 241 (2000) 166.
[2] F. Voort, Structure 28 (1995) 8.
[3] V. Teixeira, Surf. Coat. Technol. 146–147 (2001) 79.
[4] H.C. Chen, E. Pfender, J. Heberlein, Thin Solid Films 293 (1997) 227.
[5] R.W. Smith, R. Novak, PMI, Powder Metall. Int. 23 (1991) 147.
[6] H.D. Steffens, K. Nassenstein, PMI, Powder Metall. Int. 25 (1993) 280.
[7] D.Z. Guo, F.L. Li, J.Y. Wang, J.S. Sun, Surf. Coat. Technol. 73 (1995) 73.
[8] D.A. Stewart, P.H. Shipway, D.G. McCartney, Surf. Coat. Technol. 105 (1998) 13.
[9] S. Stewart, R. Ahmed, Surf. Coat. Technol. 172 (2003) 204.
[10] K.A. Khor, Mater. Manuf. Process. 12 (2) (1997) 291.
[11] K.A. Khor, Y.W. Gu, Mater. Lett. 34 (1998) 263.
[12] J. Nerz, B. Kushner, A. Rotolico, J. Therm. Spray Technol. 1 (2) (1992) 147.
[13] R. Tourret, E.P. Wright, International Symposium: I. Petroleum, Heyden and Son, London, 1977.
[14] R. Ahmed, M. Hadfield, J. Therm. Spray Technol. 11 (2) (2002) 1.
[15] R. Ahmed, M. Hadfield, Wear 220 (1998) 80.
[16] K.L. Johnson, Contact Mechanics 1st ed., Cambridge Univ. Press.
[17] C.J. Li, A. Ohmori, Y. Harada, J. Therm. Spray Technol. 5 (1996) 69.
[18] H.L. de Villiers Lovelock, J. Therm. Spray Technol. 7 (3) (1998) 357.
[19] H.C. Lee, J. Gurland, Mater. Sci. Eng. 33 (1978) 125.
[20] J. Gurland, Practical Applications of Quantitive Metallography,

American Society for Testing and Materials, Philadelphia, 1986, p. 39.
[21] T. Tomita, et al., Mechanisms of High Hardness in Cr_3C_2–NiCr Cermet Coatings Formed by Vacuum Plasma Spraying, Thermal Spray 2001: New Surfaces for a New Millennium, ASM International, Materials Park, OH, USA, 2001, p. 699.
[22] R. Okada, M. Yamanda, Trans. Jpn. Inst. Met. 58 (7) (1994) 763.
[23] D. Zhang, M. Kato, K. Nakasa, K. Tasaka, J. Mater. Sci. Soc. Japan 48 (9) (1999) 1065.
[24] J.J. Conway, B.A. Hann, ASME 384 (1999) 91.
[25] T.E. Tallian, ASME, 1999, p. 179.
[26] N.P. Suh, Wear 44 (1997) 1.
[27] J.W. Flemming, N.P. Suh, Wear 44 (1977) 39.
[28] N.P. Suh, N. Saka, Fundamentals of Tribology, Int. Conf. on the Fundamentals of Tribology, The MIT Press, 1980, p. 493.
[29] N.P. Suh, Tribophysics, Prentice-Hall, New York, 1986.
[30] R.C. Tucker Jr., J. Vac. Sci. Technol. 11 (1994) 725.
[31] E. Way, J. Appl. Mech. 2 (1935) A49.